Proton-Coupled Electron-Transfer Dynamics of Water Splitting at N-doped Graphene Oxides

Fabian Weber,[†,¶] Jean Christophe Tremblay,[‡] and Annika Bande[*,†]

†*Department of Locally Sensitive and Time-Resolved Spectroscopy, Helmholtz-Zentrum Berlin für Materialien und Energie GmbH, Hahn-Meitner-Platz 1, 14109 Berlin, Germany*

‡*Laboratoire de Physique et Chimie Théoriques, CNRS/Université de Lorraine – UMR7019, 1 Bd Arago, 57070 Metz, France*

¶*Institute of Chemistry and Biochemistry, Freie Universität Berlin, Arnimallee 22, 14195 Berlin, Germany*

E-mail: annika.bande@helmholtz-berlin.de

Abstract

In this contribution, the proton-coupled electron-transfer process in optimized nitrogen-doped graphene oxide (NGO) model catalysts is studied by means of atomistic simulations. The NGO optimization reveals that especially stabilization of a co-planar water-catalyst complex, as well as electron-withdrawing ketone groups are key features for promoting the initial charge-transfer at excitation wavelengths as low as 341.2 nm. A new model to simulate the dynamics of the overall proton-coupled electron-transfer process in an electron dynamics framework including non-adiabatic decay channels is introduced. Numerical dynamical simulations reveal that an intricate balance between the lifetime associated to vibrational dissipation (i.e. electron-phonon coupling) in the NGO model and the proton-coupled electron-transfer rate determines the overall water-splitting efficiency. October 30, 2019

keywords: molecular modelling, electron dynamics, nitrogen-doped graphene oxide, proton-coupled electron-transfer, water splitting

Introduction

In light of the ever-growing demand for energy generation it has become a central challenge to find more resource-friendly and sustainable ways to generate power. Abstractly speaking, this translates to the goal of finding new processes and materials that generate power using only abundant, non-toxic materials and available sources of energy, while causing only minimal amounts of waste. Although several working prototype methods have been found in the fields of both photovoltaics[1,2] and photochemisty,[3,4,11] none of them can so far compete with current non-sustainable energy generation techniques in terms of power output and production cost. If we therefore additionally desire a comparable efficiency, this adds to the problem the (arguably much harder to fulfil) economic requirements of minimising the costs and time per generated unit of energy while ensuring reliability and accessibility of distribution grids all around the clock.

Considering the possible energy sources, solar energy has become the most extensively studied candidate due to potentially meeting the required output and providing the necessary longevity as a sustainable resource. Although not available at all times to every part of the planet, the solar power of approximately 120 PW[5] hitting our planet could in principle easily cover for the current total energy consumption of roughly 160 PWh[6] per year. One particularly appealing route of harvesting solar energy is via the photochemically driven water splitting reaction, in which sunlight is used for converting water into its components hydrogen and oxygen. Here, the generated hydrogen can be used for producing energy-rich hydrocarbon fuels from carbon compounds[7] similar to an artifical photosynthesis. Since most energy distribution grids in use are based on hydrocarbon combustion, photochemical generation of such fuels therefore offers a most promising way of storing solar energy in a readily useful form that would not require the simultaneous re-design of current power distribution systems.

The formal oxidation and reduction part reactions of the overall water splitting require the transfer of a total of four electrons from water-bound oxygen onto water-bound protons.

$$\text{Oxidation :} \quad 2\ H_2O \quad \rightarrow \quad O_2 + 4e^- + 4H^+$$

$$\text{Reduction :} \quad 4H^+ + 4e^- \quad \rightarrow \quad 2\ H_2$$

However, the requirements for steering this process and the exact interactions between photocatalyst and environment are an ongoing topic of scientific research. The role of the photocatalyst is clearly to promote both the electron-transfer from the water-bound oxygen, as well as the transfer of a water-bound proton. This specific part reaction, which is known as the proton-coupled electron-transfer (PCET)[8,9] has been shown to greatly depend on both a suitable electronic structure for efficient charge separation, as well as the vibration dynamics when considering the transfer of the proton between water and the catalyst. Also, it has been established that this initial activation of the water-catalyst complex is the rate determining step for the overall water splitting, since all following part reactions seem to proceed much faster and without an activation barrier.

Two closely related material classes that are known to undergo this kind of reaction are graphitic carbon-nitrides[10] and nitrogen-doped graphene oxides (NGO).[11] By theoretical studies of the smaller building blocks of carbon-nitride it was found that the nitrogen atoms at the edge of the graphitic sheets act as the proton-accepting units, while the π-network of the carbon-nitride can accept the electron from the water molecule and delocalize it over the molecule.[12,13]

While there are several studies on graphitic carbon-nitrides, the closely related material nitrogen-doped graphene oxide (NGO) has not been studied in a similarly exhaustive way, yet. Although the exact oxygen functionalization pattern is hard to determine,[14,15] there are studies for improving the PCET activity that highlight the importance of binding the dopant nitrogen atoms and functional groups at the edges of the graphitic sheets.[16] This indicates that for NGOs, the PCET mechansim may be working in a similar way as in carbon nitrides.

More interestingly, the effects of the randomized nature of oxygen frunctionalization patterns on its water splitting capabilities are still unclear. To therefore establish a basic understanding for the structure-property relationships in this material class, time-dependent density functional theory (TDDFT) calculations[17] are applied on a large catalogue of differently functionalized NGO model structures to determine their electron-transfer properties. After finding a candidate model that shows a desirable charge transfer state for an absorption in the visible range, we study the PCET dynamics that comprise the first partial step of the water splitting mechanism by applying time-dependent configuration-interaction electron dynamics calculations in the reduced density matrix formulation (ρ-TDCI).[18] Here, thermal vibronic dissipation for the process is included by assuming coupling strengths that reflect different timescales for the fastest possible thermalization time. Additionally, we include coupling hydrogen transfer channels, effectively describing PCET dynamics. This way we can study which order of magnitude for non-adiabatic coupling strengths would be favourable when trying to maximize the PCET rate in an example NGO model.

The article is structured as follows. In section "Procedure and Computational Methods", we give a detailed description of the approaches and theoretical methods used in this work. In the results section, we then show the optimized candidate molecule and explain the structure-property relationships that leads to its performance with respect to excitation (sections "Structural Optimization" and "Relaxed Reaction Path of the Water Dissociation"). Finally, the PCET dynamics are discussed in section "Quantum Dynamics" for different excitation fields and vibronic coupling strengths and the effects of non-adiabatic couplings are discussed.

Procedure and Computational Methods

Optimization of the Model System

To study the photocatalytic water splitting capability of NGO model systems under irradiation with visible light, the first task is to find a reasonably small model system with at least

one charge transfer (CT) state in which an electron is shifted from the water molecule onto the NGO catalyst. Under optimal conditions, the associated excitation wavelength should be close to the maximum intensity of the sunlight emission spectrum at roughly 500 nm,[19] while also showing a high excitation probability, i.e. a high transition dipole moment.

We find such a candidate model system by systematic optimization of the oxygen functionalization pattern on a singly nitrogen-doped, coronene-sized carbon scaffold with one adsorbed water molecule facing the dopant nitrogen atom. This means that several possible locations and types of functionalizations are probed while gradually increasing the oxygen content in the model system. In all these models, the position of the nitrogen atom is kept at the edge position of the candidate structures, since this position has been confirmed as a reasonable reaction site for PCET in other nitrogen-doped molecules.[12,13] To avoid calculation of the complete chemical space of all possible functionalization patterns, a strategy based on rating functions and general chemical intuition was applied when selecting the probed patterns. Naturally, the results and design principles obtained this way will therefore only represent a subset of the overall chemical space of possible configurations.

For determining the CT properties of each candidate structure, *ab-initio* calculations are performed with the ORCA program package.[20,21] In a first step, a density-functional theory (DFT) structure optimization with one water molecule placed close to the NGO-nitrogen is carried out with the CAM-B3LYP functional[22] and the def2-SVP[23] basis set. As further corrections, we utilize Grimme's D3 dispersion correction with Becke-Jones damping[24,25] and add an implicit water environment via the conductor-like polarizable continuum model (CPCM).[28] For speeding up the calculations, the RIJCOSX method[26] is applied in combination with the respective def2-SVP/J auxiliary basis sets.[27]

After geometry optimization, time-dependent density-functional theory (TDDFT) calculations are applied to obtain the properties of the first 100 excited states of the model molecules. These calculations are performed with the same functional and parameters as the geometry optimization, but employ the diffuse def2-SVPD basis set.[29] As has been found

for the graphitic carbon nitrides, the addition of such diffuse basis functions is essential for the correct description of Rydberg-like excited states and the long-distance charge transfer states of water and the NGO molecule.[12]

CT State Characterization and Rating

To choose the best candidate among all probed molecules, a characterization and rating scheme is applied. For this purpose, we first need to quantify the degree to which an excited state describes a charge transfer from water onto the NGO catalyst. For each excited state n, the natural transition orbitals (NTO)[30] are therefore calculated from the respective transition density matrices T^n with elements T^n_{ia}, describing the excitation from the ground state wavefunction Ψ_0 as

$$T^n_{ia} = \sum_\sigma \langle \Psi_n | c^\dagger_{i\sigma} c_{a\sigma} | \Psi_0 \rangle \tag{1}$$

The indices i and a are associated with occupied and virtual molecular orbitals, respectively. Performing a singular value decomposition of the single particle transition density matrices, $T^n = U\Lambda V^\dagger$, yields two orthogonal transformation matrices U and V. These can then be used to construct the excited state in the NTO representation of hole and particle basis wavefunctions ψ^h and ψ^p.

$$\psi^h_j = \sum_i U_{ij}\phi^o_i \qquad \psi^p_j = \sum_i V_{ij}\phi^v_i \tag{2}$$

$$\Psi^h_n = \sum_j \Lambda_{jj}\psi^h_j \qquad \Psi^p_n = \sum_j \Lambda_{jj}\psi^p_n \tag{3}$$

Here, index j runs over all eigenfunctions in the NTO basis and i runs over all occupied (o) and virtual (v) molecular orbitals, respectively. The sum of the respective basis functions with their individual coefficients Λ from the singular value decomposition then yield the total

hole and particle wavefunctions Ψ_n^h and Ψ_n^p for excitation to state n.

To quantify how strongly a CT state transfers one electron from water onto the NGO catalyst, we introduce a metric based on Mulliken projectors. We calculate the hole localization on the water molecule as the expectation value of the hole wavefunction projected onto the atomic basis functions that belong to the water molecule, $\hat{P}_{\mathrm{H_2O}}$. In turn, the particle wavefunction is then projected on all remaining atomic orbitals of the NGO using $\hat{P}_{\mathrm{NGO}} = 1 - \hat{P}_{\mathrm{H_2O}}$, to yield a measure of the particle localization on the NGO. The product of both expectation values yields a measure of the overall CT purity D_n^{CT} of state n that may vary between 0 and 1,

$$D_n^{\mathrm{CT}} = \langle \Psi_n^h | \hat{P}_{\mathrm{H_2O}} | \Psi_n^h \rangle \langle \Psi_n^p | \hat{P}_{\mathrm{NGO}} | \Psi_n^p \rangle \tag{4}$$

This way, a large D_n^{CT} is obtained when the hole is localized on the water molecule and the particle is localized on the NGO model molecule for state n. After identifying the CT states with highest D_n^{CT} among the excited states, each model molecule's water splitting capabilities are rated based on a combination of the excitation energy E_{CT} closest to the sun's emission spectrum, the CT purity D_n^{CT} and the respective transition dipole moments. The rating function F is of the form

$$F = D_n^{\mathrm{CT}} \ \mu_{0n} \ B_\lambda(\lambda_n, T) \tag{5}$$

Here, D_n^{CT} is the CT purity of the energetically lowest lying CT state that shows a purity of at least $D_n^{\mathrm{CT}} > 0.7$ and μ_{0n} is the associated absolute transition dipole moment between ground and excited state. Finally, the function B_λ is the black body radiation intensity at the excitation wavelength λ_n at temperature T

$$B_\lambda(\lambda, T) = \frac{2hc^2}{\lambda^5} \frac{1}{e^{hc/\lambda k_B T} - 1} \tag{6}$$

When using a temperature of 5800 K, one qualitatively obtains the spectral intensity

distribution of sunlight.[19] Consequently, the rating function F assumes large values for pure CT states that have high transition dipole moments and a favourable excitation energy with respect to the sunlight spectrum.

Dissipative Many-Electron Dynamics

For the most promising model molecule, an analysis of the many-electron dynamics is performed to understand the timescales of electronic excitation and hydrogen transfer processes in NGO catalysts. The separate reaction channels with their respective rates Γ relevant for the PCET dynamics simulation are schematically depicted in figure 1.

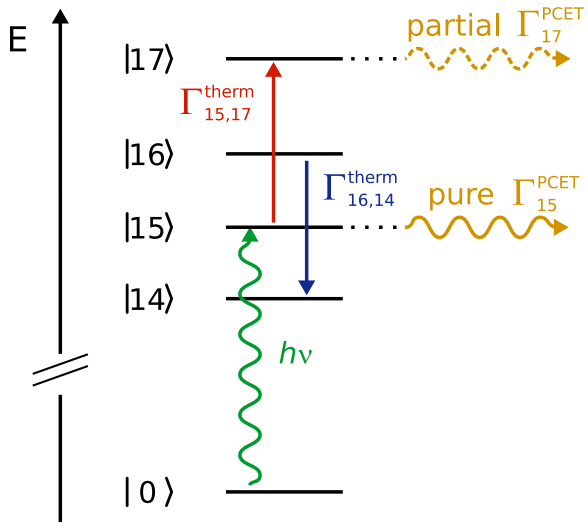

Figure 1: Schematic depiction of the reaction channels related to the PCET dynamics between electronic states $|n\rangle$. The green wavy line ($h\nu$) depicts the external field excitation. Straight vertical lines are thermal (de)excitation in blue and red, respectively. The proton-coupled electron-transfer processes (yellow) lead away horizontally from the ground state geometry. The rate of hydrogen-transfer is modulated by the charge transfer purity D_n^{CT} (see section "Hydrogen Transfer Rate"), leading to lower rates for partial charge transfer (dashed yellow) than for pure charge transfer states.

Firstly, the initial vertical excitation is driven by an external field (shown in fig. 1 with a green wavy arrow) that excites the ground state $|0\rangle$ to a mixture of excited states $|n\rangle$. These states in turn may then horizontally leave the system via PCET channels (yellow wavy arrows) that are a combination of the inverse hydrogen transfer time and the purity D_n^{CT} of

the respective CT state (see equation 12 below). Finally, all states may exchange population via thermalization (red and blue arrows). These thermalization channels allow excited states without an PCET channel to undergo a secondary PCET process via exchanging population with PCET-active states. The details of how we obtain these rates, as well as how to drive the quantum dynamics calculation with implicit vibration-induced relaxation and hydrogen-transfer will be summarized below.

Time-dependent Configuration Interaction Theory

Dissipative electron dynamics is studied here by means of the time-dependent configuration interaction method[31–33] in its reduced density matrix formulation (ρ-TDCI).[18] Formally, a basis of many-electron pseudo-eigenstates is used to represent the reduced density matrix (RDM) of the N-electron system as

$$\hat{\theta}(t) = \sum_{mn} \theta_{mn}(t)|\psi_m\rangle\langle\psi_n| \tag{7}$$

The many-electron pseudo-eigenstates are computed from time-dependent density functional theory (TDDFT) and approximated as linear combinations of singly-excited configuration state functions, $|\Phi_a^r\rangle$,

$$|\psi_n\rangle = A_0\Phi_0 + \sum_{ar} A_a^r|\Phi_a^r\rangle \tag{8}$$

In the present work, the coefficients A_a^r for the excitation from an occupied orbital a to a virtual orbital r are obtained by re-orthonormalizing the many-body pseudo-eigenstates from a TDDFT calculation at the optimal ground state geometry of the system. This hybrid TDDFT/CI formalism was shown to provide good energetics in similar charge transfer systems while retaining the computational scaling of the configuration interaction singles method.[34–36]

The RDM evolves according to the Liouville von Neumann equation

$$\frac{\partial\hat{\theta}(t)}{\partial t} = -\frac{i}{\hbar}\left[\hat{H}_{el},\hat{\theta}(t)\right] - \frac{1}{\hbar}\left[\hat{W},\hat{\theta}(t)\right]_{+} + \frac{i}{\hbar}\left[\vec{\hat{\mu}}\cdot\vec{F}(t),\hat{\theta}(t)\right] + \mathcal{L}_D\hat{\theta}(t) \tag{9}$$

where $\hat{H}_{el}$ is the Hamiltonian of the N-electron system, and the third term on the right-hand-side represents the coupling of the molecular dipole $\vec{\hat{\mu}}$ with a time-dependent external field $\vec{F}(t)$. The second term involves the anti-commutator over an absorbing potential which mimics the loss-of-norm due to hydrogen transfer, as will be discussed below. Assuming Markovian interaction with the environment, the dissipative Liouvillian super-operator in its Linblad form reads

$$\mathcal{L}_D\hat{\theta}(t) = \sum_{mn}\frac{\Gamma_{mn}}{2}\Big(\left[\hat{C}_{mn},\hat{\theta}(t)\hat{C}^{\dagger}_{mn}\right] + \left[\hat{C}_{mn}\hat{\theta}(t),\hat{C}^{\dagger}_{mn}\right]\Big) \tag{10}$$

where $\hat{C}_{mn} = |\psi_n\rangle\langle\psi_m|$ are so-called Lindblad operators that mediate the transfer from state ψ_m to ψ_n at a rate $\Gamma^{\text{therm}}_{mn}$, introduced in the next subsection. Using ansatz (7) for the RDM leads to linear equations of motions that can be integrated numerically using a pre-conditioned adaptive step-size Runge-Kutta algorithm,[37] as implemented in GLOCT.[18,38] All matrix elements required for propagating the RDM are computed from the pseudo-eigenstates, Eq. (8), using the open-source post-processing program package ORBKIT.[36,39,40] To model the behaviour of isotropic orientation in solution, all results are averaged over excitations using pulses polarized along the three cardinal directions $\{x, y, z\}$.

Vibration-induced Energy Relaxation

Non-adiabatic coupling to the system vibrations leads to energy relaxation and thermalization among the many-electron states used to represent the RDM. By using first-order time-dependent perturbation theory it was shown that energy relaxation induced by electron-vibration coupling approximately scales as the inverse of the square of the energy difference between two electronic states.[41] Here, the non-adiabatic relaxation rate Γ_{mn} between electronic states m and n is computed as the sum of the individual contributions of each vibra-

tional mode q, subject to Lorentzian broadening

$$\Gamma_{mn}^{\text{therm}} = \gamma \sum_q \left| \frac{(\gamma/2)^2}{(\Delta E_{mn} - \hbar\omega_q)^2 + (\gamma/2)^2} \right| \text{ , with } E_m > E_n \tag{11}$$

The upward rates are obtained by detailed balance, $\Gamma_{nm}^{\text{therm}} = e^{E_{mn}/K_b T} \Gamma_{mn}$. These are required, since we consider the system at finite the temperature $T = 300$ K. The normal mode frequencies ω_q are obtained from numerical vibrational analysis of the NGO candidate molecule at the ground state geometry, while the ΔE_{mn} are the associated electronic energy differences from the excited states at the same geometry. The parameter γ is introduced as a measure for the maximum possible relaxation rate from state n to m via non-adiabatic coupling, and its effect on the many-electron dynamics will be discussed below. Additionally, the parameter is directly related to a relaxation lifetime via the Lorentzian width.

Hydrogen Transfer Rate

Provided the molecule is electronically excited to a CT state, the water molecule is expected to fragment into a hydroxyl radical and a hydrogen atom that is transferred to the NGO catalyst. This hydrogen transfer from water to NGO is expected to strongly impact the laser excitation dynamics and compete with vibronic relaxation induced by non-adiabatic coupling (i.e. thermalization). To provide a combined picture of electronic excitation and hydrogen transfer dynamics, we introduce in Eq. (9) a negative imaginary potential of the form

$$\hat{W} = \sum_n \Gamma_n^{\text{PCET}} |\Psi_n\rangle\langle\Psi_n| = \frac{D_n^{\text{CT}}}{\tau_n^{\text{HT}}} |\Psi_n\rangle\langle\Psi_n| \tag{12}$$

where τ_n^{HT} is the duration associated with the hydrogen transfer process. The role of this imaginary potential is to absorb the outgoing flux of hydrogen, which ultimately reduces the overall norm of the wavefunction. Assuming that the reaction is completely irreversible, the loss of norm yields a measure for the rate of combined electron and hydrogen transfer

dynamics - i.e. the PCET process. Since the desired final product is an uncharged hydroxyl and NGO+H complex that can only be obtained from an equally strong proton and electron transfer (i.e. the pure charge transfer case of $D_n^{\mathrm{CT}} = 1$), the rate at which a given state n is annihilated, $1/\tau_n^{\mathrm{HT}}$, is modulated by its CT character D_n^{CT}, obtained from the previous NTO analysis (see Eq. (4)). This will be discussed in more detail in the results section.

We estimate the decay time τ^{HT} from the vibrational period of the atom on the lowest-lying charge transfer state with the highest D_n^{CT}. A relaxed reaction path (RRP) for the water splitting reaction of the candidate NGO system is first constructed by performing constrained structure optimizations of the ground state DFT level (cf. section "Relaxed Reaction Path of the Water Dissociation") where the O-H bond of the water molecule facing the nitrogen is constrained to different lengths. Subsequent TDDFT calculations at each of these geometries yield potential energy curves of multiple electronically excited states along the reaction coordinate. The first pure CT state, identified by following the energetically lowest lying state with the largest D_n^{CT} along the RRP, is then fitted to a harmonic potential centered at proton transfer geometry. We define the decay time for the hydrogen transfer τ_n^{HT} as the time required for the hydrogen atom (mass $M = 1.00797$ a.m.u.) to decay towards the minimum of the pure CT state, starting from the pure CT state in the ground state geometry. Throughout all subsequent electron dynamics simulations, the hydrogen transfer time estimate of $\tau_n^{\mathrm{HT}} = 7\,\mathrm{fs}$ is used.

Results and Discussion

Structural Optimization

The NGO model molecule developed in this study is obtained after five stages of successive functional group addition to the N-doped coronene base structure (total number of 158 model structures, see ESI for more information). The excitation properties of the most suitable candidate at each stage are collected in table 1 and figure 2 shows which structural features

were added at each stage. The final candidate NGO model shows an extended π-conjugated network that contains two ketone groups (stages one and two), as well as one carboxyl group (stage three). This special arrangement allows the water molecule to be hydrogen-bonded in co-planar fashion to both one of the carboxyl oxygen atoms as well as the ketone oxygen added in stage one. Further, the electron withdrawing effects of the oxygen atoms overall facilitate the transfer of a p-electron from the water molecule to the π-system of the NGO molecule, effectively red-shifting the excitation wavelength for the pure CT state from 186.3 nm in the unfunctionalized pristine case to 341.2 nm in the proposed candidate NGO model (compare table 1).

By addition of the epoxy group to the model molecule at stage four, the excitation wavelength is again red-shifted, while however strongly lowering the transition dipole moment. Therefore, although the phenol group of stage five slightly blue-shifts the excitation wavelength and lowers the charge transfer purity D_n^{CT} for the pure CT state, it causes a much better transition dipole moment again - which is why this last modification still provides an improvement. It shall also be noted that the introduction of hydroxyl groups saturating a π-bond with -OH and -H generally leads to a blue-shift of the excitation wavelength for almost all probed cases. Since a blue-shift of the excitation energy will lead away from the optimum of 500 nm, this indicates hydroxyl groups are unfavourable for optimising the electron-transfer properties.

Among the first 100 excited states of the final candidate molecule, only the two states number 15 and 80 (numbering according to the ORCA [20] output) qualify as pure charge transfer states with D_n^{CT} of at least 0.70. Besides these two, there exist ten additional states with D_n^{CT} values of at least 0.10, which shall be referred to as partial CT states in the following.

The hole and particle NTO wavefunctions (cf. equation 2) that describe the pair of energetically lowest-lying partial and pure CT states are shown in figure 3. From these NTO wavefunctions one can see that the hole wavefunction of the partial CT state 14 is

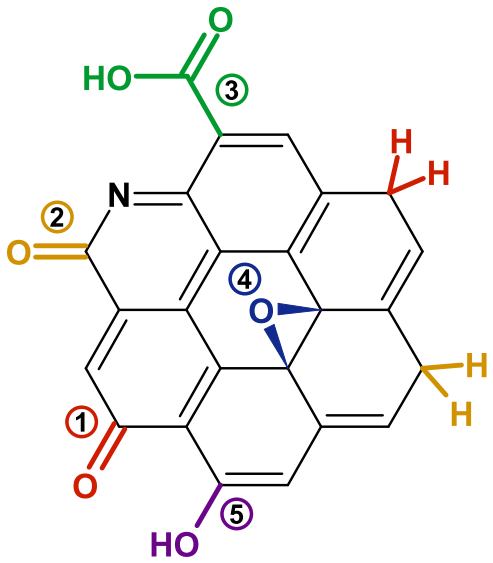

Figure 2: Development of the final candidate molecule. Numbers and colors indicate what changes were introduced in which stage.

also localized on the NGO catalyst's carboxyl group, while the pure CT state 15 shows an almost exlcusive localization on the water molecule. Note that the numbering of states according to ORCA[20] is not necessarily ordered energetically. The particle wavefunctions of both pure and partial CT states are essentially identical and spread over the π-conjugated ketone groups and adjacent pristine C atoms. This analysis of the electronic structure in terms of energies and densities has already several implications for the molecular design principles of efficient NGO catalysts. Firstly, it shows that the charge transfer to the NGO can be facilitated by adding electron-withdrawing substituents to the π-system, because it lowers the energy of the particle wavefunction. However, due to the particle wavefunctions being so similar for partial and pure CT states, such adjustments result in a red-shift for the excitation wavelength of both the partial as well as pure CT states in comparable magnitude.

Secondly, since the hole wavefunction is the only substantial difference between the partial and pure CT state's NTOs, the only way of favouring a pure CT over partial CT is to disfavour the partial CT state's hole wavefunction. In the proposed final candidate structure (as shown in figures 2 and 3), this is achieved by a push-pull asymmetry introduced with the carboxyl group, relative to the ketones. While the carboxyl group is electron-rich, it is

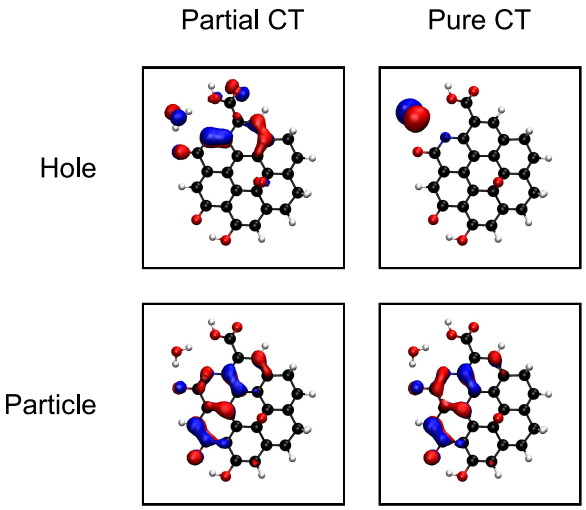

Figure 3: Hole and particle wavefunction of the energetically lowest-lying partial CT state 14 and pure CT state 15 in a contour plot with a cutoff of ±0.05.

Table 1: Charge transfer characteristics of the different generations of NGO model molecules. Numbers in parentheses reflect states that come closest to the pure/partial state description, while missing the requirement of $D_n^{\mathrm{CT}} > 0.70$ and $D_n^{\mathrm{CT}} > 0.10$, respectively.

Development Stage	**exc. wavelength pure/part. [nm]**	D_n^{CT} **pure/part.**	$\lvert\vec{\mu_{0n}}\rvert^2$ **pure/part. [au]**
Pristine	186.3 / 170.5	0.75 / 0.18	1.18 / 2.07
Stage 1	(238.7) / (298.9)	(0.66) / (0.08)	(0.01) / (0.01)
Stage 2	(270.1) / 263.3	(0.38) / 0.22	(0.001) / 0.08
Stage 3	329.0 / (306.6)	0.89 / (0.03)	0.05 / (0.04)
Stage 4	344.4 / (310.0)	0.93 / (0.02)	0.03 / (0.02)
Stage 5	341.2 / 276.6	0.89 / 0.14	0.08 / 0.39

also electrophilic, thus disfavouring the formation of a hole in this region. This is reflected by the large drop in D_n^{CT} of the lowest partial CT state from stage two to three (see table 1).

Finally, it shall be noted that the arrangement of the water molecule with respect to the NGO seems to be important for the CT process. While the water molecule is rather randomly oriented with respect to the O-H-N bond in the first stages of the candidate development, all of the 16 structures of the last functionalization stage only feature a co-planar arrangement and two O-H-O hydrogen bonds instead.

Relaxed Reaction Path of the Water Dissociation

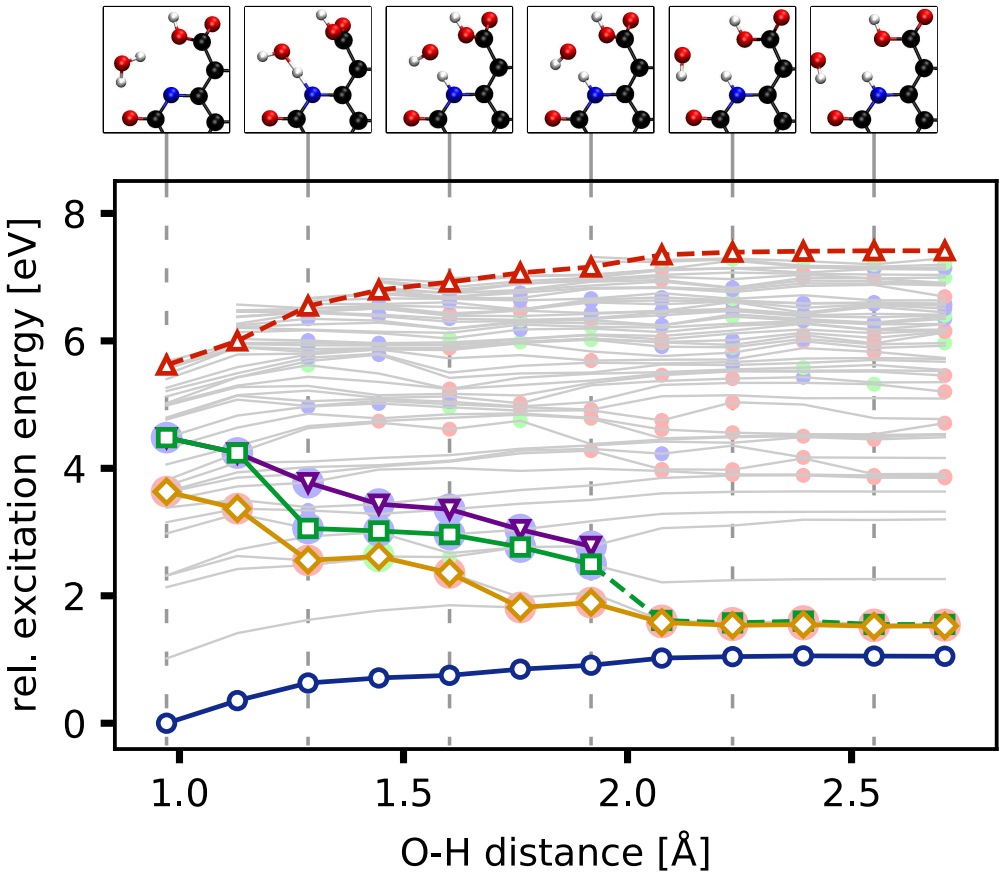

Figure 4: Relative energies of the electronic ground state (blue circles), lowest-energy pure CT (yellow diamonds) and partial CT states (green squares and violet downwards triangles) and the ionization limit (red upwards triangles) as function of the O-H bond distance. Additionally, the adiabatic states are shown in the background according to their energetic ordering at each geometry with gray thin lines. Colored dots highlight states of pure ($D_n^{\mathrm{CT}} > 0.7$, red), intermediate partial ($0.7 > D_n^{\mathrm{CT}} > 0.5$, green) and partial CT character ($0.5 > D_n^{\mathrm{CT}} > 0.1$, blue) The NGO+H active site geometries are displayed in the upper panels at selected distances.

The RRP was obtained by a constrained geometry optimization of the NGO water complex, where the O-H bond closer to the NGO nitrogen was elongated in sequential steps. The upper panels of figure 4 show cutouts of the molecular structures featuring the elongation of the O-H bond that eventually leads to the formation of an N-H bond between the NGO and the former water-proton. The proton transfer is accompanied by a rotation of the carboxyl group around the distance of 1.4 Å, such that the repulsion by the free electron pairs of the

water-oxygen is minimized. In the lower panel of figure 4, the relative energies of the ground state (blue circles), as well as the energetically lowest lying partial and pure CT states (green squares and yellow diamonds, respectively) are given along the relaxed reaction path (i.e. O-H distances). Note that state numbers may change between geometries due to state crossings or changes in CT character. Consequently, only the energetically lowest-lying pure as well as a pair of partial CT states are highlighted by following the dominant charge transfer numbers at each of the geometries. Further, the CT states are labelled at each geometries according to their strength, separated in pure CT ($D_n^{\mathrm{CT}} > 0.7$, red), intermediate partial CT ($0.7 > D_n^{\mathrm{CT}} > 0.5$, green), and weak partial CT ($0.5 > D_n^{\mathrm{CT}} > 0.1$, blue). Finally, the ionization limit (red triangles) is estimated from the cation energy at the same geometry.
As one can see, the dissociation of the O-H bond is energetically unfavourable in the electronic ground state (blue circles) since the energy increases along the reaction coordinate. For the pure and partial CT states (yellow diamonds and green squares/violet triangles, respectively) the dissociation is favourable, thus confirming the general possibility of driving the PCET reaction after excitation into such states. The dynamical behaviour in the partial and pure CT states is nonetheless expected to be different. At a distance approaching 1.3 Å, the hydrogen atom becomes shared between the nitrogen atom of the NGO and the OH fragment. This leads to a mixing of the state characters, as seen from the reduction of the CT purity D_n^{CT}. The partial CT character is also spread over many states, bracketed by the green and violet lines. This strong character mixing implies that hopping between these states will occur rapidly, leading to an overall return of the hydrogen towards the original NGO+water conformation. This can be inferred from the behaviour of the adiabatic potential energy curves in grey, that all favor this conformation. On the contrary, the pure CT state has little overlap with all other states in this energy window due to its very different character. The branching ratio for dynamics in this state will thus be strongly biased towards the hydrogen transfer, as coupling to the states favoring the original NGO+water conformation is weak. This branching ratio can be included in the dynamics by modulating the PCET

rate according to the degree of charge transfer D_n^{CT}, as described in the theory section.

For distances larger than 1.92 Å, the partial (dashed line) and pure CT states energies become almost identical. This energy convergence towards the pure CT state is caused by the partial CT states splitting, with one adopting a pure CT character beyond this distance. The reason for this can be understood from the changes in the bonding situation: While the pure CT related electron originates from the p orbital perpendicular to the H-O-H plane (cf. figure 3), the in-plane p orbitals are used for forming the O-H bonds. For longer O-H distances, however, one of the in-plane p orbitals is now available for donating an electron to the NGO catalyst molecule, as well. This behaviour can be confirmed by analyzing the D_n^{CT} values at the different distances for both the pure and partial CT states (see figure 5a)). Here, one finds that for larger distances the partial CT states D_n^{CT} values (green squares) approach the pure CT state beyond a distance of 2.0 Å. Additionally, there is a local minimum in the pure CT and local maximum in the partial CT states' D_n^{CT} close to an O-H distance of 1.5 Å, which is indicative of either a local avoided crossing or a conical intersection between the potential energy surfaces of partial and pure CT states around that distance.

Since the ground and CT states become energetically close for large O-H distances, there is in principle a possibility for either of the states to return to the ground state potential energy surface and thus towards the undesired initial reactand geometry. When analyzing the absolute transition dipole moment $|\mu_{0n}|^2$ for the partial and pure CT states in figure 5b), however, one notes that with increasing distances, it becomes smaller and smaller, making a return to the ground state potential surface less likely. Finally, we indirectly confirm the biradical final product at approximately 2.6 Å by analyzing the Mulliken charge of the fragments of the electronic ground state (figure 5c)). The fragments were chosen such, that the oxygen and hydrogen of the former water molecule build up one fragment (OH), and the NGO molecule and the transferred hydrogen build up the other (NGO+H). Since the OH fragment (red triangles) shows a negative charge and the NGO+H complex (blue circles) a positive one at the largest separation, the charge transfer states that purely transfer one

electron from the OH fragment onto the NGO+H complex need to be charge-neutral on each fragment.

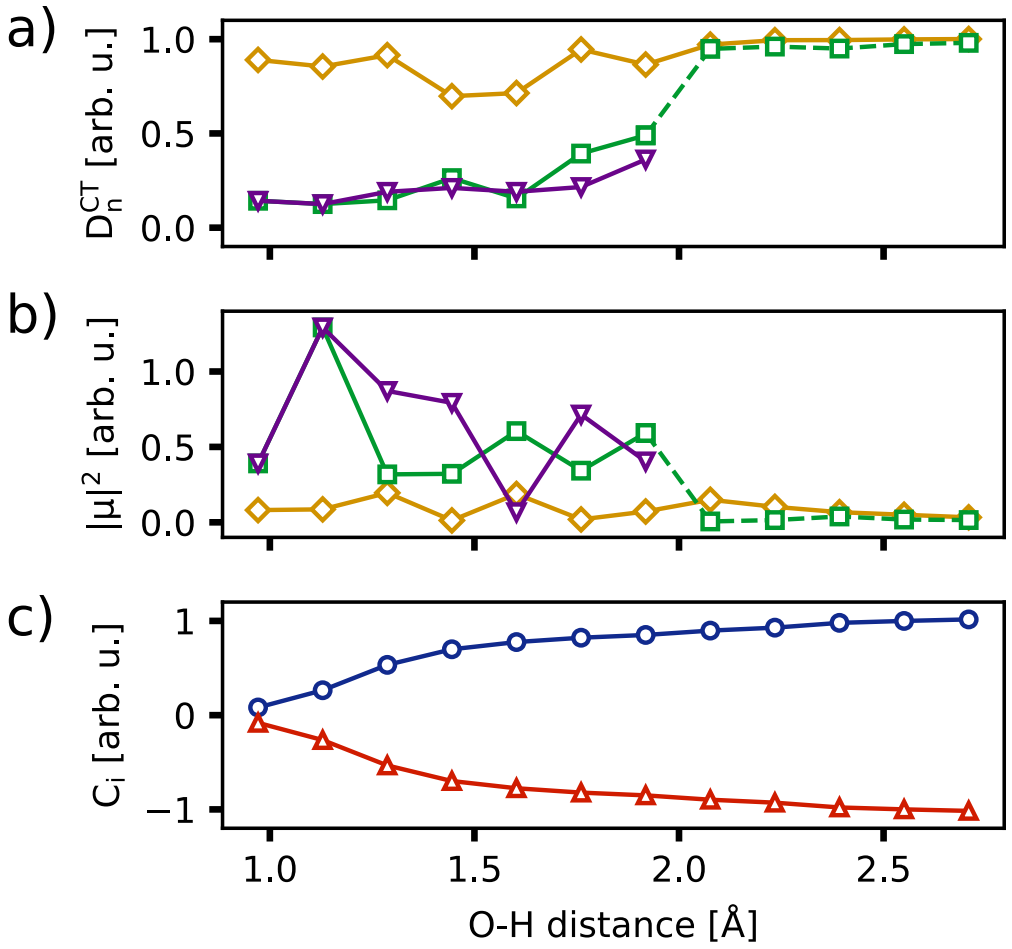

Figure 5: D_n^{CT} values (a) and magnitude of the transition dipole moments $|\mu_{0n}|^2$ (b) for transition from ground state into the pure (yellow diamonds) and partial CT states (green squares and purple triangles) at different OH bond lengths. Panel (c): Partial Mulliken charges C_i on the NGO+H fragment (blue circles) and OH fragment (red triangles) are given for the electronic ground state.

Quantum Dynamics

The quantum dynamics for the PCET step of the water splitting reaction can be treated in an explicit electron dynamics framework with implicit nuclear dynamics implemented through the hydrogen transfer rate $\frac{1}{\tau_n^{\mathrm{HT}}}$ as introduced in section "Dissipative Many-Electron Electron Dynamics". In the following, we shall split the discussion of our findings into one

section for the dynamics during the initial excitation pulse and one section for the dynamics after the pulse. In all cases, the state populations shown below are an average for three individual excitation dynamics with linearly x, y and z polarized external fields. This way, the behaviour of an isotropic arrangement of NGO-water complexes is obtained.

To test the behaviour of the NGO-water complex for various excitations, different parametrizations for both the external field as well as the non-adiabatic thermalization rate γ are used. For the external field, the numbers chosen mimic readily available laboratory lasers. We probe three different pulse lengths t_s (25, 50 and 100 fs) and two different amplitudes (0.001 au and 0.01 au). Since the amplitudes translate to relatively weak peak intensities of 3.51×10^{12} and 3.51×10^{13} W/cm^2, respectively, we do not expect that ionization with respect to multi-photon processes play a role for the dynamics. The frequency of the carrier pulse is fixed to 0.134 au (341.2 nm), which corresponds to the excitation energy of the lowest lying pure CT state (see Table 1).

The thermalization rates γ, were chosen such that the minimal thermalization time $\tau_\gamma = \frac{1}{\gamma}$ of each individual vibration channel corresponds to 10, 1 and 0.1 ps, respectively. These translate to testing cases of weak, intermediate, and strong non-adiabatic coupling between the electronic states with respect to molecular vibrations. In all cases, the propagation after the laser pulse was continued until the respective thermalization time τ_γ.

Initial Excitation Dynamics

In the following, the simulations for using a pulse length of 50 fs shall be discussed in detail. The results of other laser set-ups may be taken from table S.II in the electronic supplementary material. To understand the trends for the dynamics during the external field excitation for different PCET scenarios, we discuss the left halves of figures 6a-f). Here, panels a-c) correspond to the external field amplitude with 3.51×10^{12} W/cm^2 peak intensity (shown in the background in light gray), while panels d-f) reflect scenarios with 3.51×10^{13} W/cm^2 peak intensity. Each panel contains information about the time-dependent norm

(black), ground state population (blue) as well as the sum over all pure and partial CT state populations (orange and green, respectively). Additionally, the sum of excited states that cannot decay via hydrogen transfer (furthermore called "non-CT states" with $D_n^{\mathrm{CT}} < 0.1$) is given as a dashed gray line. Note that the populations of partial and pure CT states were scaled for better readability. The panels of each column differ by their thermalization times that can be found in the lower left corner of each panel.

From panels a-c one can see that in the initial excitation period of 50 fs the norm stays virtually the same for all values of τ_γ, while the ground state populations decrease in a similar fashion in all three cases by about 13%. The lost ground state population is almost exclusively transferred to non-CT states in all three cases (note the scaling by a factor 1000 for the CT states). This shows that during excitation using a weak pulse, no norm-reducing PCET occurs, although the excitation frequency is tuned resonant with the lowest lying pure CT state. The reasons are twofold: First, the imaginary potential term associated with each partial and pure CT state (cf. equation 12) effectively changes the energetic resonance condition for the laser excitation, thus leading to a lowered transition probability in general. Second, due to the ultrafast hydrogen transfer rates ($\frac{1}{7\mathrm{fs}} = 0.14\mathrm{fs}^{-1}$), population of these states would be immediately removed, leading to an immediate decrease in the wavepacket norm. The ultrafast hydrogen transfer rate also has the nefarious effect of inducing dephasing between the ground and CT states on the same femtosecond timescale. As the initial and final states lose their coherence due to this dephasing, population transfer via coherent laser interaction with light becomes almost impossible. The inefficiency of the excitation process can be overcome by a stronger perturbation of the system. Therefore, it is only around the laser field peak intensity, when the excitation probability bebcomes higher than the PCET rate, that population of pure CT states can be observed.

When focusing on the populations of the partial CT states, one sees that the cases of weak and intermediate vibronic coupling (panels a) and b), respectively) strongly differ from the case of strong vibronic coupling (panel c)). While the populations stop increasing

after the maximum laser amplitude for a) and b), it continues growing over a much longer time and to a higher overall value for scenario c). The reason for this difference is most likely connected to the different thermalization rates between states compared to the PCET rates of the partial CT states: In scenarios a) and b) the fastest thermalization rates are of the order of $\Gamma_{mn} = 0.1\text{ps}^{-1}$, which is relatively slow compared to the partial PCET rates $\frac{D_n^{\text{CT}}}{\tau^{\text{HT}}} = \frac{0.1}{7fs} = 0.014\text{fs}^{-1}$. Therefore, after the population via the laser becomes slower than the PCET rate, the partial CT populations start to monotonously decrease. In case of strong vibronic coupling, however, the fastest thermalization rates between states are of the order of magnitude 0.01fs^{-1}, therefore potentially competing with some of the partial CT channels.

When using lasers with higher peak intensities, d-f), one can see a much more pronounced depopulation of the ground state to approximately 0.4, associated with an immediate loss of norm. However, due to fast decoherence between the ground and CT states as discussed above, most of the excited population is still transferred to non-CT states. As was the case for weaker intensity pulses, the three regimes of vibronic coupling strengths show no strong differences in the behaviour of the norm, the ground state, and the non-CT populations.

Although the partial and pure CT state populations are overall much higher compared to excitations with weak laser fields, the three cases behave similar to each other with respect to these PCET-active states. Again, one notices that the partial CT state population in Fig. 6f) is much higher for short thermalization times (note the different scaling factor for the green and orange curves). However, one also notices that the pure CT states show a different behaviour for the strong vibronic coupling case, since its peak population is even less than half of the peak population in the other two coupling regimes. The reason for this may be that the PCET rates become comparable to that of the thermalization. Since it is hard to see from the panels a-c), this behaviour cannot be confirmed for the weaker external field.

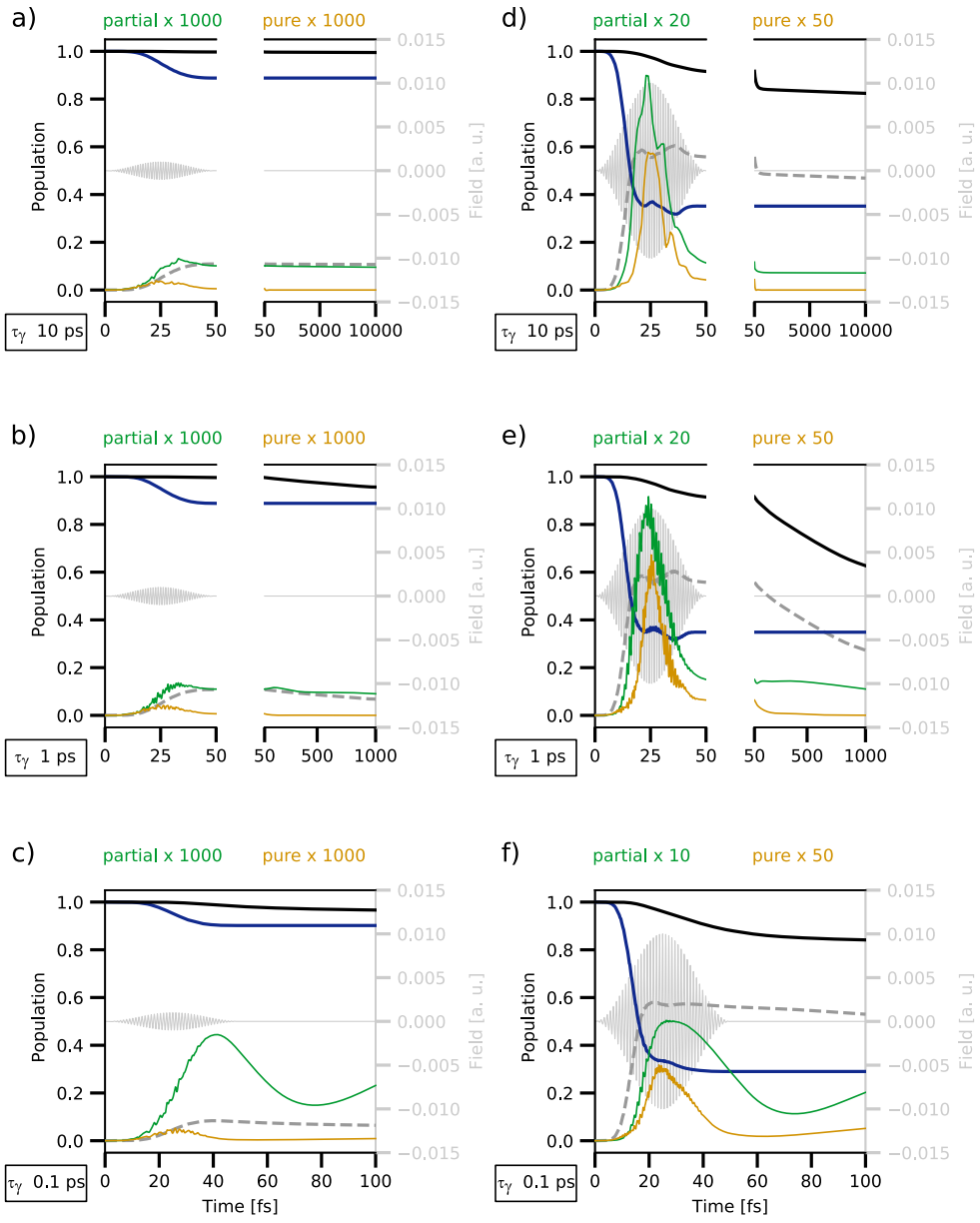

Figure 6: Model PCET dynamics for excitation with different external field amplitudes and thermalization times τ_γ. Shown are the norm (black), ground state (blue) as well as the sums of all pure CT states (orange) and partial CT states (green) as a function of time. The external field is shown in light grey with respect to the second y-axis. The sums of pure and partial states were scaled for better readability as indicated above the panels. Note, that some pictures have been split into an excitation period and post-excitation period.

Thermalization Dynamics

Next, we focus on the dynamics after the laser excitation for the scenarios depicted in the right halves of figures 6a-f). First, one notices that regardless of the thermalization

parameter, the ground state population does not change with time in any of the scenarios. The reason is that the energetic difference between the ground and excited states is too large to be overcome for any of the probed vibronic coupling strengths. While the transfer rates between ground and excited states are indeed finite and non-vanishing, they tend to be of the orders of $\approx 10^{-12}$ fs^{-1} (i.e. 1 s^{-1}) and are therefore not noticeable on the probed timescales.

When focusing on the cases of lasers with low peak intensities a-c), one finds that for the weak and intermediate vibronic coupling strengths (panels a) and b)), the partial and pure CT state populations stay virtually constant as well. While the pure CT states start off the thermalization dynamics with virtually zero population, the partial CT states are re-populated through thermalization at a similar rate as their PCET decay. Eventually, for very high thermalization rates, scenario c) even shows an increase of the partial CT states population close to the end of the propagation. This can be explained by the thermalization rates that become competitive with the PCET rates.

When turning to the thermalization-induced norm loss, we note that for $\tau_\gamma = 1$ ps (panels b) and e)), the norm loss is the highest. We further notice that it is almost the same as the decrease in the sum of all non-CT states, indicating that the losses are caused by secondary processes – i.e. non-PCET states populating partial or pure CT states, that may then decay through the hydrogen transfer channel (see section "Dissipative Many-Electron Electron Dynamics").

The same behaviour for both the state populations as well as the norm loss can be found for the higher amplitude excitation scenarios d-f), albeit in a much more pronounced fashion. Especially for the intermediate vibronic coupling scenario shown in panel e), the final norm is at 0.63 – indicating that almost half of the NGO-water complexes have initiated a PCET process after the simulation time of 1 ps. Again, a high efficiency of the secondary PCET for the non-CT states can be observed.

Since neither the partial nor the pure CT state populations change drastically, it is reasonable to assume that the important thermalization processes leading to the secondary

PCET are of the same order of magnitude as their connected PCET channels. Also, since the faster hydrogen transfer time for a pure CT state is 7 fs while the shortest possible thermalization time is of the order of 1 ps for this case, one would expect that the secondary decay channels causing the norm loss need to be connected to "non-CT $\rightarrow$ weak partial CT $\rightarrow$ hydrogen transfer" processes rather than to pure CT states when following the same timescale difference argument as discussed for the excitation dynamics.

To prove this hypothesis, the thermalization rates for the most prominent excited non-CT states are compared with the rates of their respective target PCET channels. To find which states are the most prominent, a series of thermalization dynamics with initial population in each of the individual excited non-CT state is performed. This allows to extract the state-specific norm losses originating from thermalization processes. Weighting each state-specific norm loss with the state populations at the end of the laser pulse in the actual dynamics, the non-CT states can be sorted according to their importance for the secondary PCET.

Fig. 7 depicts the detail of the thermalization dynamics for scenario e). The bold gray dashed line represents the sum of all non-CT states that decrease at almost identical rate than the overall norm (black line). When taking the seven non-CT states with the highest importance for the secondary PCET (thin colored lines), one may decompose the gray line further into the sum of important (dashed blue line) and unimportant non-CT states (dashed red line). The blue dashed line again decreases similarly to the gray one while the red dashed line follows a slower decay. This is indicative that the excited non-CT states with higher secondary PCET efficiency are responsible for the observed norm loss. Note that the blue line converges monotonically to the gray dashed line when including more partial contributions.

Analyzing individual thermalization rates $\Gamma_{mn}^{\mathrm{therm}}$ (cf. equation 11) of the seven dominant states m towards all other states n, one recognizes that the timescales for thermalization and hydrogen transfer processes are of similar magnitude in some cases. In particular, states 7, 58, 63, and 64 have PCET rates of a few picoseconds, comparable with the thermalization regime $\tau_\gamma = 1\mathrm{ps}$. However, these states have almost no initial population and therefore

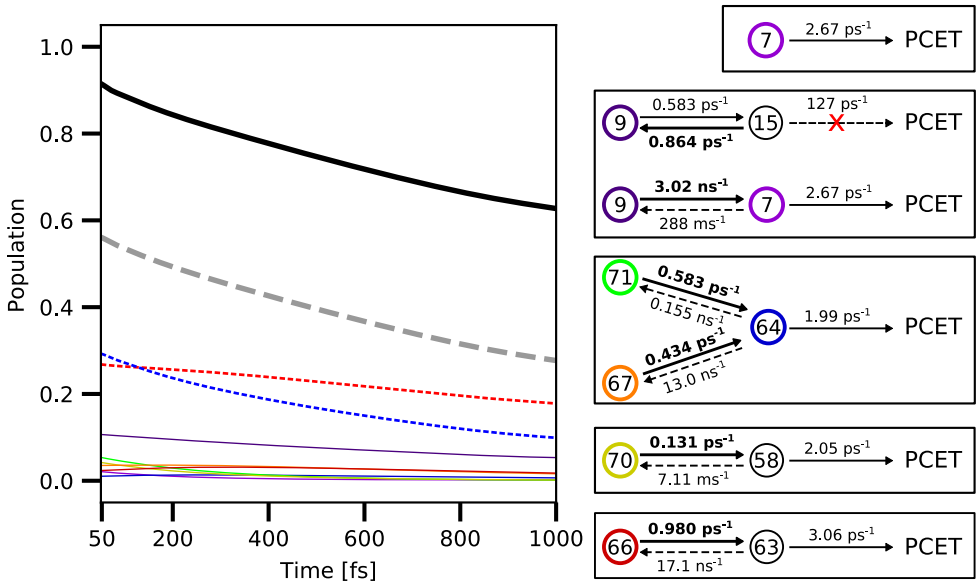

Figure 7: Left panel: Detailed thermalization dynamics for τ_γ=1 ps and peak intensity 3.51 10^{13} W/cm^2 (as in figure 6e)). The bold black line represents the norm of the wavefunction, and the gray dashed line represents the sum of all non-CT states. The thin solid lines represent the seven most important non-CT states that decay via secondary processes. The thin dashed blue and red lines give the sum of these seven states and all remaining non-CT states, respectively. Right panel: Secondary hydrogen transfer channels of the seven most important non-CT states. Circled numbers refer to the n-th electronic state, numbers above the arrows reflect the individual thermalization/PCET rates. The bold circles are color-coded as the populations in the left panel.

do not strongly contribute to the decay in a direct PCET process. They are, however, suitable for *indirect* PCET decay via secondary thermalization from neighbouring excited non-CT states. After the pulse of 50 fs duration, direct PCET has contributed to the depopulation of the short-lived CT states and only partial CT-states remain populated. The dominant contributions stem from states 9, 66, 67, 71, and 72 in the case presented in Fig. 7. The equilibrium for these states is strongly biased towards states 7, 58, 63, and 64, which present a thermal stability comparable to their PCET rates. Consequently, PCET and further thermalization become competitive, which explains why this specific choice of pulse duration and thermalization rate leads to the highest light-to-proton transfer efficiency, as documented by the largest overall loss-of-norm after thermalization. In general, these considerations explain why both lower or higher thermalization times τ_γ potentially lead to

less secondary thermalization norm loss. For $\tau_\gamma = 10$ ps, the thermalization rates become too slow compared to even the lowest hydrogen transfer rates, and the populations remain trapped in the states or slowly return to the global ground state. On the other hand, for a lower $\tau_\gamma = 0.1$ ps, thermalization becomes too fast and dominates PCET, while reducing the excitation probability by increasing the dephasing rate.

It can be inferred from these simulations that the efficiency of the PCET process can be enhanced by optimizing the non-adiabatic couplings of the electron dynamics to the NGO phonons, such as to maximize the relative importance of the secondary PCET process induced by thermalization.

Conclusion

In this work we provide a detailed discussion of the proton-coupled electron-transfer (PCET) dynamics for the water splitting by as nitrogen-doped graphene oxide (NGO) model molecule. In a first step, we determine important functionalization patterns that facilitate the initial charge transfer (CT) step from water onto NGO. It is observed that a π-conjugated network of electron-withdrawing groups is important for stabilising the particle wavefunction on the NGO catalyst such that the excitation wavelength shifts form the ultraviolet regime towards the visible light spectrum. Additionally, a co-planar arrangement of the water molecule is found to be important for lowering the excitation energy further.

Using an optimized model containing all important molecular features for the charge transfer state, the dissociative nature of the charge transfer states is confirmed by calculating the reaction pathway for the hydrogen transfer reaction. The dissipative many-electron dynamics of the proton-coupled electron-transfer is studied by means of the time-dependent configuration interaction in its reduced density matrix variant (ρ-TDCI). The coupling of the electron dynamics to the phonons of the NGO model is computed from normal mode analysis and using a phenomenological scaling constant that determines the thermalization

timescale in the system. The vibrational lifetime of the pure charge transfer state, which is found to be ~ 7 fs, is used to define a hydrogen transfer rate. It enters the dynamics as a loss-of-norm channel, which quantifies the efficiency of the hydrogen transfer process. The computational setup allows simulating laser excitations of a water NGO complex at finite temperatures, as well as the PCET and thermalization dynamics, to determine their relative timescale and efficiency.

From these simulations, we find that applying a short field at relatively high peak intensity leads to a important norm loss in the water NGO complex of 0.09 directly after the laser pulse. It is also observed that thermalization of longer-lived partial charge transfer states can increase the PCET yield on the picosecond timescale. For the optimal combination found in this work (50 fs pulse with 3.51 10^{13} W/cm^2 peak intensity and a thermalization rate $\tau_\gamma = 1\,\text{ps}$), slightly more than a third of an ensemble of NGO-water complexes would undergo water splitting at room temperature. Comparing these timescales to the ultrafast hydrogen transfer time in a CT state, we observe that the rate of water splitting is strongly limited by the efficiency of the initial optical excitation, largely due to the rapid dephasing in the system. An intricate balance between non-adiabatic thermalization pathways and the hydrogen transfer indicates the importance of considering temperature and vibronic coupling in the design of such materials for applications in nanoscopic devices. From the probed vibronic coupling strengths, we conclude that thermalization lifetimes of the order of 1 ps are desirable for devices that are operating at room temperature. The thermalization lifetime, which is related to phonon lifetimes, could be controlled by optimizing dopant and defect concentrations in NGO catalysts, as well as by modifying the size of the active site.

Acknowledgements

We thank the Volkswagen foundation for financial support (Freigeist Fellowship No. 89525).

References

(1) Yoshikawa, K., Kawasaki, H., Yoshida, W., Irie, T., Konishi, K., Nakano, K., Uto, T., Adachi, D., Kanematsu, M., Uzu, H., Yamamoto, K. Silicon heterojunction solar cell with interdigitated back contacts for a photoconversion efficiency over 26%. *Nature Energy* **2017**, *2*, 17032.

(2) Gaspar, H., Figueira, F., Pereira, L., Mendes, A., Viana, J. C., Bernardo, G. Recent Developments in the Optimization of the Bulk Heterojunction Morphology of Polymer: Fullerene Solar Cells. *Materials* **2018**, *11*, 2560.

(3) Mosconi, D., Mazzier, D., Silvestrini, S., Privitera, A., Marega, C., Franco, L., Moretto, A. Synthesis and Photochemical Applications of Processable Polymers Enclosing Photoluminescent Carbon Quantum Dots. *ACS Nano* **2015**, *9*, 4, 4156.

(4) Testa, C., Zammataro, A., Pappalardo, A., Sfrazzetto, G. T. Catalysis with carbon nanoparticles. *RSC Adv.* **2019**, *9*, 27659.

(5) Morton, O. A new day dawning? Silicon Valley sunrise. *Nature* **2006**, *443*, 7107, 19.

(6) BP Statistical Review of World Energy 2019 (BP, **2019**); https://www.bp.com/content/dam/bp/business-sites/en/global/corporate/pdfs/energy-economics/statistical-review/bp-stats-review-2019-full-report.pdf (Accessed Sep. 7th, 2019).

(7) Chang, X., Wang, T., Gong, J. CO2 photo-reduction: insights into CO2 activation and reaction on surfaces of photocatalysts. *Energy Environ. Sci.* **2016**, *9*, 2177.

(8) Hammes-Schiffer, S. Proton-Coupled Electron Transfer: Moving Together and Charging Forward. *J. Am. Chem. Soc.* **2015**, *137*, 8860.

(9) Shimizu, T., Sugiura, M., Noguchi, T. Mechanism of Proton-Coupled Electron Transfer

in the S0-to-S1 Transition of Photosynthetic Water Oxidation As Revealed by Time-Resolved Infrared Spectroscopy. *J. Phys. Chem. B* **2018**, *122*, 9460.

(10) Wang, X., Maeda, K., Thomas, A., Takanabe, K., Xin, G., Carlsson, J.M., Domen, K., Antonietti, M. A metal-free polymeric photocatalyst for hydrogen production from water under visible light. *Nature Materials* **2009**, *8*, 76.

(11) Yeh, T.-F., Cihlář, J., Chang, C.-Y., Cheng, C., Teng, H. Roles of graphene oxide in photocatalytic water splitting. *Mater. Today* **2013**, *16*, 78.

(12) Ehrmaier, J., Karsili, T. N. V., Sobolewski, A. L., Domcke, W. Mechanism of Photocatalytic Water Splitting with Graphitic Carbon Nitride: Photochemistry of the Heptazine-Water Complex. *J. Phys. Chem. A* **2017**, *121*, 4754.

(13) Ehrmaier, J., Janicki, M. J., Sobolewski, A. L., Domcke, W. Mechanism of photocatalytic water splitting with triazine-based carbon nitrides: insights from ab initio calculations for the triazine–water complex. *Phys. Chem. Chem. Phys.* **2018**, *20*, 14420.

(14) Dreyer, D. R., Park, S., Bielawski, C. W., Ruoff, R. S. The chemistry of graphene oxide. *Chem. Soc. Rev.* **2010**, *39*, 228.

(15) Weber, F., Ren, J., Petit, T., Bande, A. Theoretical X-ray absorption spectroscopy database analysis for oxidised 2D carbon nanomaterials. *Phys. Chem. Chem. Phys.* **2019**, *21*, 6999.

(16) Chang, D. W., Baek, J.-B. Nitrogen-Doped Graphene for Photocatalytic Hydrogen Generation. *Chem. Asian J.* **2016**, *11*, 1125.

(17) Runge, E., Gross, E. K. U. Density-Functional Theory for Time-Dependent Systems. *Phys. Rev. Lett.* **1984**, *52*, 997.

(18) Tremblay, J. C., Klamroth, T., Saalfrank, P. Time-dependent configuration-interaction

calculations of laser-driven dynamics in presence of dissipation. *J. Chem. Phys.* **2008**, *129*, 084302.

(19) Delgado-Bonal, A. Entropy of radiation: the unseen side of light. *Sci. Rep.* **2017**, *7*, 1642.

(20) Neese, F. The ORCA program system. *WIREs Comput Mol Sci* **2012**, *2*, 73.

(21) Neese, F. Software update: the ORCA program system, version 4.0. *WIREs Comput Mol Sci* **2018**, *8*, 1327.

(22) Yanai, T., Tew, D. P., Handy, N. C. A new hybrid exchange–correlation functional using the Coulomb-attenuating method (CAM-B3LYP). *Chem. Phys. Lett.* **2004**, *393*, 51.

(23) Schäfer, A., Horn, H., Ahlrichs, R. Fully optimized contracted Gaussian basis sets for atoms Li to Kr. *Chem. Phys.* **1992**, *97*, 2571.

(24) Grimme, S., Antony, J., Ehrlich, S., Krieg, H. A consistent and accurate ab initio parametrization of density functional dispersion correction (DFT-D) for the 94 elements H-Pu. *J. Chem. Phys.* **2010**, *132*, 154104.

(25) Grimme, S., Ehrlich, S., Goerigk, L. Effect of the Damping Function in Despersion Corrected Density Functional Theory. *J. Comput. Chem.* **2011**, *32*, 1456.

(26) Neese, F., Wenmohs, F., Hansen, A., Becker, U. Efficient, approximate and parallel Hartree–Fock and hybrid DFT calculations. A 'chain-of-spheres' algorithm for the Hartree–Fock exchange. *Chem. Phys.* **2009**, *356*, 98.

(27) Weigend, F. Accurate Coulomb-fitting basis sets for H to Rn. *Phys. Chem. Chem. Phys.* **2006**, *8*, 1057.

(28) Cossi, M., Rega, N., Scalmani, G., Barone, V. Energies, Structures, and Electronic Properties of Molecules in Solution with the C-PCM Solvation Model. *J. Comput. Chem.* **2003**, *24*, 669.

(29) Rappoport, D., Furche, F. Property-optimized Gaussian basis sets for molecular response calculations. *J. Chem. Phys.* **2010**, *133*, 134105.

(30) Martin, R. L. Natural transition orbitals. *J. Chem. Phys.* **2003**, *118*, 4775.

(31) Klamroth, T. Laser-driven electron transfer through metal-insulator-metal contacts: Time-dependent configuration interaction singles calculations for a jellium model. *Phys. Rev. B* **2003**, *68*, 245421.

(32) Vanne, Y.V. and Saenz, A. Numerical treatment of diatomic two-electron molecules using a B-spline based CI method. *J. Phys. B: At. Mol. Opt. Phys.* **2004**, *37*, 4101.

(33) Greenman, L., Ho, P.J., Pabst, S., Kamarchik, E., Mazziotti, D.A., Santra, R. Implementation of the time-dependent configuration-interaction singles method for atomic strong-field processes. *Phys. Rev. A* **2010**, *82*, 023406.

(34) Hermann, G., Tremblay, J.C. Ultrafast photoelectron migration in dye-sensitized solar cells: Influence of the binding mode and many-body interactions. *J. Chem. Phys.* **2016**, *145*, 174704.

(35) Klinkusch, S., Tremblay, J. C. Resolution-of-identity stochastic time-dependent configuration interaction for dissipative electron dynamics in strong fields. *J. Chem. Phys.* **2016**, *144*, 184108.

(36) Hermann, G., Pohl, V., Tremblay, J.C. An open-source framework for analyzing N-electron dynamics. II. Hybrid density functional theory/configuration interaction methodology. *J. Comput. Chem.* **2017**, *38*, 2378.

(37) Tremblay, J. C., Carrington Jr., T. Using preconditioned adaptive step size Runge-Kutta methods for solving the time-dependent Schrödinger equation. *J. Chem. Phys.* **2004**, *121*, 11535.

(38) Tremblay, J.C., Klinkusch, S., Klamroth, T., Saalfrank, P. Dissipative many-electron dynamics of ionizing systems. *J. Chem. Phys.* **2011**, *134*, 044311.

(39) Hermann, G., Pohl, V., Tremblay, J.C., Paulus, B., Hege, H.-C., Schild, A. ORBKIT: A modular python toolbox for cross-platform postprocessing of quantum chemical wavefunction data. *J. Comput. Chem.* **2016**, *37*, 1511.

(40) Pohl, V., Hermann, G., Tremblay, J.C. An open-source framework for analyzing N - electron dynamics. I. Multideterminantal wave functions. *J. Comput. Chem.* **2017**, *38*, 1515.

(41) Hermann, G., Tremblay, J. C. Laser-Driven Hole Trapping in a Ge/Si Core-Shell Nanocrystal: An Atomistic Configuration Interaction Perspective. *J. Phys. Chem. C* **2015**, *119*, 25606.